


Consistent Assessment of Microwave Scattering and Vertical Dynamic Characteristics in the Precipitation Environment Over Oceans

Yuxuan Feng , Jieying He , *Member, IEEE*, Gang Ma , Jing Huang, Jingyang Li , Yang Guo , Guiqing Liu, Peng Zhang , *Senior Member, IEEE*, and Jiandong Gong

Abstract—To improve the assimilation accuracy of satellite microwave observations, it is necessary to conduct precipitation detection before assimilation and exclude the data contaminated by the scattering of hydromorphic particles. The induction of microwave scattering is closely related to the effective radius of hydromorphic particles, and the motion state of hydromorphic particles at different scales can directly affect the internal dynamic structure of clouds, which will lead to precipitation. To further analyze and validate the impact of microwave scattering in a precipitation environment on the assimilation of satellite microwave soundings within the temperature-sensitive band, this article utilized the on-orbit observations of Microwave Temperature Sounder-III (MWTS-III) and Medium Resolution Spectral Imager onboard the Fengyun-3E (FY-3E) satellite to achieve multispectral fusion observation and precipitation detection over oceans, combined with the vertical dynamic characteristics of global numerical forecast in the cloud environment of China Meteorological Administration (CMA) Global Forecast System (CMA-GFS). By conducting the dynamic analysis of the hydrometeors in the cloud, the maximum possible effective particle radius of hydromorphic particles under the no-phase-transition condition and internal vertical motion is obtained. The consistency of the cloud liquid water path (CLWP) retrieved by MWTS-III and multispectral fusion precipitation detection is evaluated subsequently. The results show that the distribution of hydrometeors in the CMA-GFS forecast is broadly in line with the CLWP distribution obtained from the MWTS-III retrieval, regardless of Mie scattering or Rayleigh scattering. However, compared with Mie scattering, the weak convection of CMA-GFS shows better adaptability in the Rayleigh environment.

Index Terms—Consistency assessment, dynamic analysis, FY-3E MWTS-III, microwave precipitation detection, microwave scattering.

I. INTRODUCTION

SATELLITE microwave data can be used to detect the upwelling radiation attenuation caused by gas absorption at different altitudes, obtaining a vertical structure of atmospheric temperature and humidity. Compared with visible light and infrared sounding [1], microwave sounding can better describe the characteristics of the occurrence and development of weather systems [2], and has become an important way to detect the atmospheric state in cloud and precipitation environments. The research has shown that in the global numerical weather prediction (NWP) system, the forecast level will be reduced by 23.4% without assimilating satellite-sounding data, among which the forecast level will be reduced by 13.8% without assimilating microwave-sounding data [3]. It can be seen that microwave-sounding data have a positive impact on NWP.

Nevertheless, the scattering effect of large-diameter rainwater and ice particles on microwave in cloud and precipitation environments cannot be ignored. In the microwave spectrum, the atmosphere not only includes the absorption and emission phenomena of molecules such as oxygen (O_2) and water vapor (H_2O) but also involves the strong radiation and scattering effects of various hydromorphic particles [4], [5]. For spaceborne microwave sounders detecting absorption and emission of O_2 and H_2O , the scattering of hydrometeors will lead to a large deviation between the observed brightness temperature and the simulated background brightness temperature (O-B) [6], [7], which is far larger than the deviation of about $10^{-1}K$ when only molecular absorption and emission occur [8]. Therefore, to fully utilize microwave-sounding data and ensure the effect of assimilation analysis, satellite radiance data are usually assimilated after cloud and precipitation detection and elimination of observations affected by clouds and precipitation, and it has been proved by a large number of studies that it has a significant improvement on NWP [9], [10], [11]. It is necessary to differentiate the scattering of large-diameter hydromorphic particles in precipitation environments, select and eliminate observations that exhibit significant deviations caused by particle scattering to ensure high-quality satellite microwave data positively impacts global NWP operations.

Manuscript received 13 January 2024; revised 23 March 2024 and 29 May 2024; accepted 26 June 2024. Date of publication 3 July 2024; date of current version 24 July 2024. This work was supported by the Youth Cross Team Scientific Research Project of the Chinese Academy of Sciences under Grant JCTD-2021-10. (*Corresponding authors: Jieying He; Gang Ma.*)

Yuxuan Feng is with the Key Laboratory of Microwave Remote Sensing, National Space Science Center, Chinese Academy of Sciences, Beijing 100190, China, and also with the University of Chinese Academy of Sciences, Beijing 100049, China (e-mail: fengyuxuan22@mails.ucas.ac.cn).

Jieying He and Jingyang Li are with the Key Laboratory of Microwave Remote Sensing, National Space Science Center, Chinese Academy of Sciences, Beijing 100190, China (e-mail: hejieying@mirslab.cn; lijingyang@nssc.ac.cn).

Gang Ma, Jing Huang, Guiqing Liu, and Jiandong Gong are with the Center for Earth System Modeling and Prediction of CMA, Beijing 100081, China (e-mail: magang@cma.gov.cn; huangj@cma.gov.cn; liuqq@cma.gov.cn; gongjd@cma.gov.cn).

Yang Guo and Peng Zhang are with the National Satellite Meteorological Center, Beijing 100081, China (e-mail: guoyang@cma.gov.cn; zhangp@cma.gov.cn).

Digital Object Identifier 10.1109/JSTARS.2024.3422649

In determining whether the observation is affected by clouds and precipitation, it is usually considered that each channel has different sounding characteristics and the sensitivity to the scattering effects of clouds and precipitation particles is also different. When clouds and precipitation particles are present, the radiant brightness temperature observed by each channel will change differently, and based on this change, it is possible to determine whether there are clouds and precipitation particles in the atmosphere. For precipitation detection from microwave observations, the main method involves calculating the scattering index (SI) from the brightness temperature of the low-frequency channels at 23.8 and 31.4 GHz with the higher frequency channel at 89 GHz. If the SI exceeds a certain threshold, it is determined that precipitation has occurred at that pixel [12], [13]. Weng et al. regarded the CLWP retrieved from the brightness temperature of the channels at 23.8 and 31.4 GHz as a marker for microwave precipitation detection [14], [15]. This method has been applied in assimilation systems such as grid-point statistical interpolation (GSI), laying the foundation for the assimilation of spectral “equivalent clear-sky” observations [16]. Li et al. developed a new precipitation detection method based on visible and infrared radiometer (VIRR) cloud mask pixels from the MWTS-I onboard the Fengyun-3 A (FY-3 A) [17] and Fengyun-3B (FY-3B) satellite [18]. The cloud mask from VIRR is matched to the data from the MWTS-I field of view (FOV) to calculate the cloud fraction. Through a number of tests and verification with CLWP from the Meteorological Operational Satellite A (Metop-A), a reasonable threshold can be derived for precipitation detection, as an alternative to conventional precipitation detection. This method has been applied to data from the Fengyun-3 C/D (FY-3 C/D) MWTS-II in the Global and Regional Assimilation and Prediction System (GRAPES) of CMA [19]. In a similar study, Han et al. employed the high-resolution cloud products from Moderate-resolution Imaging Spectroradiometer (MODIS) and Visible Infrared Imager Radiometer Suite (VIIRS) to aid in cloud prediction using the Advanced Microwave Sounder Unit-A (AMSU-A) and the advanced technology microwave sounder (ATMS), which shows that cloud detection can be effectively carried out by using high-resolution cloud products [20]. This approach, focused on the elimination of the contaminated observational data tainted by precipitation, achieving results comparable to traditional precipitation detection methods. It can be seen that an accurate cloud and precipitation detection scheme ensures the reasonable utilization of satellite microwave-sounding data, which is an important basis to ensure the assimilation effect of satellite observations in cloud and precipitation environment.

Moreover, precipitation is closely related to water vapor, and the dynamic structure within the cloud is also a direct cause of precipitation [21]. The vertical velocity of cloud water particles in the atmosphere intuitively reflects their force and motion state in the vertical direction. The induction of microwave scattering is closely related to the effective radius of hydromorphic particles, and the effective radius of cloud water particles supported by different cloud environments varies significantly [22], [23]. Based on the fifth-generation reanalysis data (ERA5) from the European Centre for Medium-range Weather Forecasts and

precipitation observations from the global precipitation measurement satellite, the precipitation structure and cloud parameter structure were studied by Wang et al. It was found that the effective particle radius distribution aligns fundamentally with the physical inference based on cloud-physical precipitation [24]. Therefore, although the distribution of hydromorphic particles in the NWP model space is different from that in actual observations, relevant studies can be conducted in the overlapping area, which is the consistent part of the NWP model space and actual observations. For example, if we can obtain the maximum possible effective particle radius of the hydromorphic particle under the effect of vertical motion in the cloud without phase transition by analyzing the force on the hydromorphic particle in the cloud, then the consistency between the maximum possible effective particle radius and the CLWP distribution from satellite microwave precipitation detection can be analyzed.

In the precipitation environment, it is an important prerequisite for the effective assimilation of satellite data to make accurate judgments and reasonable processing of satellite observations affected by clouds and precipitation. To further analyze and validate the impact of microwave particle scattering in precipitation environments on the assimilation of microwave soundings within the temperature-sensitive band, based on the on-orbit observations of MWTS-III and MERSI carried by the FY-3E satellite and the vertical dynamic characteristics of CMA-GFS global numerical forecast in the cloud environment, the consistency of the retrieved CLWP and multispectral fusion precipitation detection distribution from FY-3E MWTS-III was evaluated in this study. The mechanism analysis methods is described in Section II. Details and specifications of the data, model, and experimental scheme are provided in Section III. The results are provided in Section IV. Section V provides a discussion and conclusion.

II. MECHANISM ANALYSIS METHODS

A. Cloud Liquid Water Algorithm for Satellite Microwave Observational Radiation

The scattering of the upwelling microwave radiation by hydrometeors in the atmosphere over the open ocean can be derived using two channels at 23.8 and 31.4 GHz [15]

$$CLWP = a_0 \mu [\ln(T_s - T_{b31}) - a_1 \ln(T_s - T_{b23}) - a_2] \quad (1)$$

where $CLWP$ is the cloud liquid water path; T_s is the sea surface temperature; T_{b23} and T_{b31} represent the observed brightness temperature at 23.8 GHz and 31.4 GHz, respectively. a_0 , a_1 , and a_2 are all related to the mass absorption coefficients of water vapor and cloud liquid water in the two channels. The coefficient μ is the cosine of the local zenith (polar) angle.

When the CLWP calculated by (1) is greater than 0.2 kg/m^2 , it is considered that the microwave radiation in the low-frequency band is contaminated by precipitation [15], [16]. If the value of CLWP is greater than 0.02 kg/m^2 , it is usually indicated that the corresponding observation is contaminated by clouds [25], [26]. To evaluate the impact of scattering on microwave precipitation detection, only cloud-contaminated MWTS-III data are studied,

observations that were not contaminated by clouds will be excluded.

B. Dynamic Analysis of Hydrometeors in Cloud Environment

The relationship between CLWP and hydromorphic particles can be expressed as [27], [28]

$$CLWP = \frac{4}{3}\rho_w\pi \int_0^z \int_0^\infty r^3 n(r) dr dz \quad (2)$$

where ρ_w is the density of liquid water and $n(r)$ is the number density of hydrometeors with radius r . The effective radius of particles is defined as follows:

$$r_e = \frac{\int_0^\infty r^3 n(r) dr}{\int_0^\infty r^2 n(r) dr}. \quad (3)$$

Assuming that there is no collision and phase transformation of hydromorphic particles during the ascending motion, the effective radius r_e does not change with altitude. When only spherical liquid water particles are considered, the effective radius of these particles in the atmosphere is equal to their spherical radius. For the area where microwave scattering occurs, the effective particle radius of hydrometeors can be obtained according to the distribution of its number density in NWP. Hydrometeors in the atmosphere are subjected to the gravity F_G and the Archimedean buoyancy force F_{static} in the vertical direction:

$$F_G = \rho_p V_p g = \rho_p \frac{4}{3}\pi R_p^3 g = \frac{4\pi}{3} g \rho_p R_p^3 \quad (4)$$

$$F_{\text{static}} = \rho_{\text{air}} V g = \rho_{\text{air}} \frac{4}{3}\pi R_p^3 g = \frac{4\pi}{3} g \rho_{\text{air}} R_p^3 \quad (5)$$

where ρ_p is the density of the hydrometeor, R_p is the radius of the hydrometeor, V_p is the volume of the spherical hydrometeor, g is the acceleration of gravity, ρ_{air} is the atmospheric density, and V is the volume of the air displaced by the spherical particle, which is equal to V_p . For an individual spherical hydromorphic particle, its buoyancy force is much smaller than its gravity. When the hydromorphic particle inducing the microwave scattering is statically suspended in the cloud and there is no phase transition, the buoyancy force can be ignored. In this condition, the force balanced with the particle's gravity is the dynamic buoyancy force generated by the upward motion of within the cloud, which can be expressed as:

$$F_{\text{dynamic}} = F_{\text{total}} - F_{\text{static}} = \frac{4\pi}{3} g (\rho_p - \rho_{\text{air}}) R_p^3 \quad (6)$$

where F_{total} is the total buoyancy force, and F_{dynamic} is the dynamic buoyancy force.

Assuming that the particle is sufficiently small and the ascending time is short enough, the vertical velocity can be expressed as

$$w \approx F_{\text{dynamic}} = \frac{4\pi}{3} g (\rho_p - \rho_{\text{air}}) R_p^3. \quad (7)$$

By substituting the radius of the hydromorphic particle obtained from (3) into (7), the vertical velocity that satisfies low-frequency microwave scattering can be calculated, and CLWP can also be calculated.

III. EXPERIMENTAL DESIGN

A. Experimental Data

1) *FY-3E MWTS-III Observations*: The channel characteristics of FY-3E MWTS-III, including center frequency, bandwidth, NEDT, and spatial resolution, are shown in Table I. FY-3E MWTS-III is equipped with 17 channels, among which the four channels at 23.8, 31.4, 53.246 ± 0.08 GHz, and 53.948 ± 0.081 GHz are newly added [29]. In this study, the Level-1c (L1c) product of FY-3E MWTS-III is provided by the National Satellite Meteorological Center (NSMC) of CMA (<http://satellite.nsmc.org.cn/portalsite/default.aspx>, accessed on 9 November 2022). This data product contains 17 channels of observed brightness temperatures from the Level-1 (L1) data product. In addition, based on the FOVs of MWTS-III, it integrates the cloud detection products from MERSI, the CLWP retrieved from MWTS-III, and the SI from MWHS-II. One of the typical variables in the FY-3E MWTS-III L1c product is the cloud fraction, which is defined as the ratio of the number of cloudy MERSI pixels in the MWTS-III FOV to the total number of MERSI pixels in the MWTS-III FOV. In this article, we used the brightness temperature and the cloud fraction from the L1c product for further research.

2) *CMA-GFS*: CMA-GFS is a multiscale generalized data assimilation and numerical forecasting system independently developed by China, which was officially put into operational use in 2016 [30], [31]. Its atmospheric model is a global, fully compressible, nonhydrostatic model utilizing vector wind, and potential temperature as independent variables. The CMA-GFS dynamic framework employs a semi-implicit semiLagrangian scheme for time integration and vector field discretization techniques for calculating the curvature term and addressing vector computational problems in the polar regions. A complete parameterization scheme of physical processes is available, including radiation, cumulus convection, cloud microphysics, boundary layer vertical diffusion, and land surface processes [32]. Its forecast setup is shown in Table II [33].

B. Experimental Scheme

The current frequency distribution of satellite microwave detectors is mainly ranging from 23.8 to 183 GHz. The effective radius of hydromorphic particles corresponding to different frequencies of radiation when scattered by hydromorphic particles is shown in Fig. 1. For 60 GHz microwave observation, the hydromorphic particles inducing scattering are generally liquid. The ratio of the radius r to the radiation's wavelength λ is known as the size parameter. When only considering the spherical liquid water particles, if we adopt $2\pi r/\lambda = 1$ and $2\pi r/\lambda = 0.1$ as the cutoff separating Mie and Rayleigh scattering, respectively [22], [23], the full Mie solution is required for sizes greater than approximately 0.80 mm at 60 GHz, the cutoff for Rayleigh solution is about 0.08 mm at 60 GHz. Assuming that the atmospheric column is filled with liquid water, integration across the entire column according to (2), $CLWP > 0.2 \text{ kg/m}^2$ indicates Mie scattering, while $CLWP > 0.02 \text{ kg/m}^2$ suggests both Mie and Rayleigh scattering are occurring simultaneously. The CLWP

TABLE I
CHANNEL CHARACTERISTICS OF FY-3E MWTS-III

No.	Center Frequency(GHz)	Bandwidth(MHz)	NEDT(K)	Spatial Resolution(km)
1	23.8	270	0.30	60
2	31.4	180	0.35	60
3	50.30	180	0.35	33
4	51.76	400	0.30	33
5	52.8	400	0.30	33
6	53.246 ± 0.08	2×140	0.35	33
7	53.596 ± 0.115	2×170	0.30	33
8	53.948 ± 0.081	2×142	0.35	33
9	54.40	400	0.30	33
10	54.94	400	0.30	33
11	55.50	330	0.30	33
12	$57.29(f_0)$	330	0.60	33
13	$f_0 \pm 0.217$	2×78	0.70	33
14	$f_0 \pm 0.322 \pm 0.048$	4×36	0.80	33
15	$f_0 \pm 0.322 \pm 0.022$	4×16	1.00	33
16	$f_0 \pm 0.322 \pm 0.010$	4×8	1.20	33
17	$f_0 \pm 0.322 \pm 0.0045$	4×3	2.10	33

TABLE II
FORECAST SETTINGS FOR THE CMA-GFS

Horizontal Distribution of Forecast Variables	Arakawa–C skip point grid
Vertical Distribution of Forecast Variables	Charney-Philips skip layer settings
Vertical coordinate	Height-based terrain-following coordinates
Horizontal resolution	$0.25^\circ/1^\circ$
Number of vertical layers	87
Height of the top of the model layer	0.1hPa
Integration time length	6 h

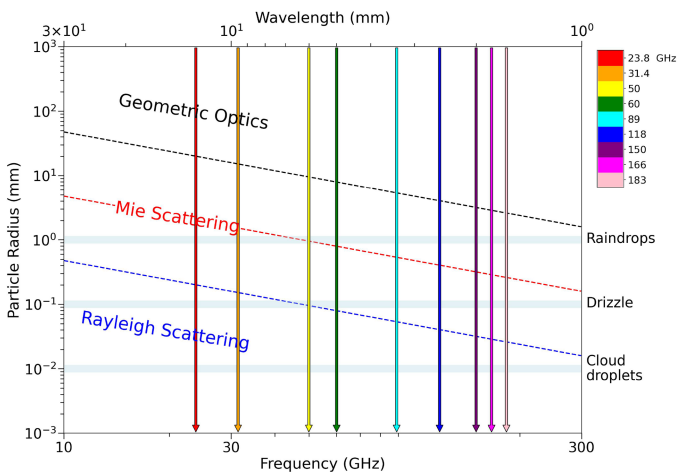


Fig. 1. Relationship between frequency and effective radius of the hydromorphic particle in the microwave spectrum from 10 to 300 GHz when subjected to scattering by these particles. The area above the black dot line means the geometric optical scattering where the particle size is many times the wavelength; the area below the blue dot line means the Rayleigh scattering; the red dot line means the Mie scattering. The three thick blue lines represent for three particle phase states: raindrops, drizzle, and cloud droplets, which is up to the particle size.

derived using (1) also uses these thresholds to identify Mie scattering and Rayleigh scattering.

Infrared and microwave spectral radiation have different penetrations through clouds and since precipitation occurs within cloud areas, infrared spectral cloud detection can serve as one of the evaluation standards for microwave precipitation detection. Therefore, in this study, the scattering distribution of MWTS-III

is examined based on the FY-3E MWTS-III observations using the MERSI cloud products matched to the MWTS-III FOV, and the dynamic characteristics of particles in NWP forecast field are further analyzed. The specific experimental steps are as follows:

Step 1: Collection of MWTS-III observations to retrieve the scattering distribution. The FY-3E MWTS-III L1c dataset from 1 September 2022, to 10 September 2022, was collected, and after sea and land identification of the brightness temperature and removal of coastline effects, the CLWP was retrieved according to the cloud liquid water algorithm. Then the pixels corresponding to Mie scattering and Rayleigh scattering were selected based on the calculated scattering threshold.

Step 2: Evaluation of MWTS-III precipitation detection with matched MERSI cloud soundings. MERSI cloud fraction data matched to MWTS-III FOVs were extracted from the 10-day FY-3E MWTS-III L1c data that have been collected, and combined with the two CLWP-scattering pixels selected in step 1, the scattering distributions of the FY-3E MWTS-III are further examined to assess the effect of MWTS-III precipitation detection.

Step 3: Using CMA-GFS to carry out the global forecast experiment. The forecast of the CMA-GFS is selected from 31 August 2022, to 9 September 2022. Forecasts were made four times daily at 6-h intervals, each lasting 24-h with hourly outputs of the 3-D distribution of hydromorphic particles. The pressure layers selected for the horizontal analysis are 300, 500, 700, and 850 hPa.

Step 4: Determine the experimental region. The NWP experimental region was determined according to the five types of hydromorphic particles, and then the scattering experimental

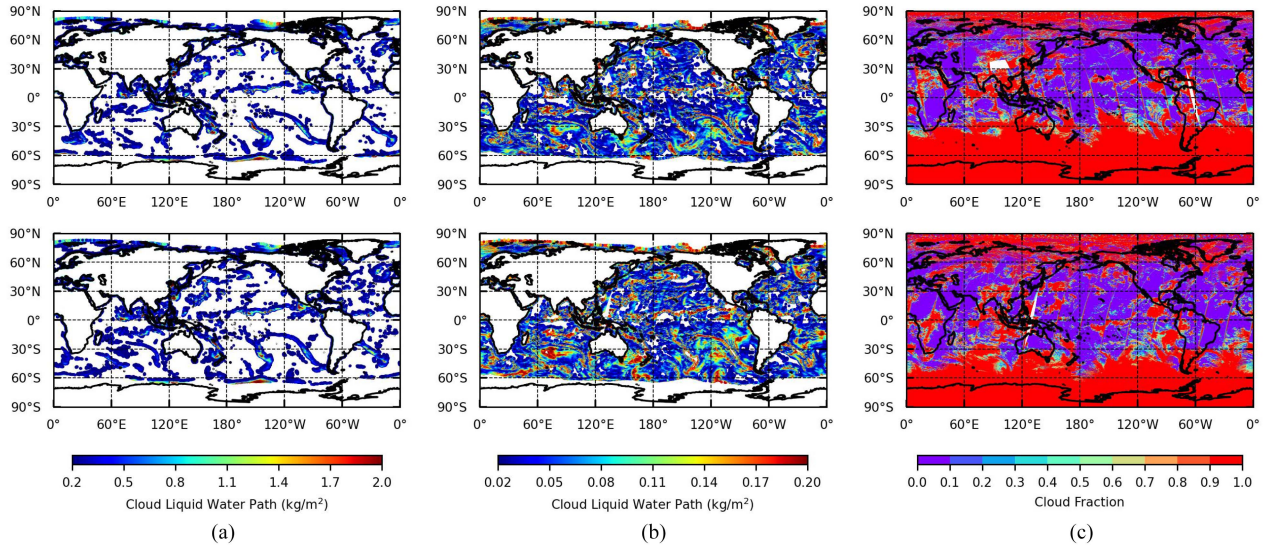


Fig. 2. Calculated (a) CLWP for Mie scattering, (b) CLWP for Rayleigh scattering, and (c) MERSI Clfra matched to MWTS-III FOVs based on FY-3E MWTS-III ascending and descending orbit observations on 4 September 2022.

region of the retrieved CLWP was combined to determine the common region of the two as the experimental region.

Step 5: Comprehensive analysis of NWP forecast and MWTS-III retrieved scattering. In the experimental region selected in Step 3, the consistency comparison analysis of one single moment, the daily variation analysis, and the 10-day time series analysis were performed for the NWP forecast and the MWTS-III retrieved scattering, respectively.

IV. ANALYSIS OF EXPERIMENTAL RESULTS

A. Evaluation of MWTS-III Precipitation Detection With Matched MERSI Cloud Detection

The CLWP calculated from the brightness temperatures observed by the 23.8 and 31.4 GHz channels of FY-3E MWTS-III over oceans for Mie and Rayleigh scattering is shown in Fig. 2(a) and (b). The cloud fraction (Clfra) rematched to MWTS-III FOVs is shown in Fig. 2(c). The value of Clfra ranges from 0 to 1, with larger values indicating more clouds. The MWTS-III spatial resolution of 33 km at nadir is not sufficient to reveal differences between broken cloud areas and clear areas, whereas the high-resolution MERSI cloud products are more accurate in cloud detections. Since precipitation occurs in the cloud area, the more clouds there are, the more hydromorphic particles there are in the cloud, and the easier it is to induce scattering. Despite the difference in resolution, the area of microwave Mie and Rayleigh scattering corresponds well to the MERSI cloud high-value regions.

Using the CLWP derived from MWTS-III FOVs and the matched MERSI Clfra from 1 September to 10 September 2022, the temporal evolution diagram of the occurrence probability of Mie and Rayleigh scattering with the matching Clfra is shown in Fig. 3. In the figure, the scattering probability for MWTS-III FOV Clfra greater than 0.6, 0.7, 0.8, 0.9, and 1.0 are derived from the ratio of the number of Mie/Rayleigh scattering pixels

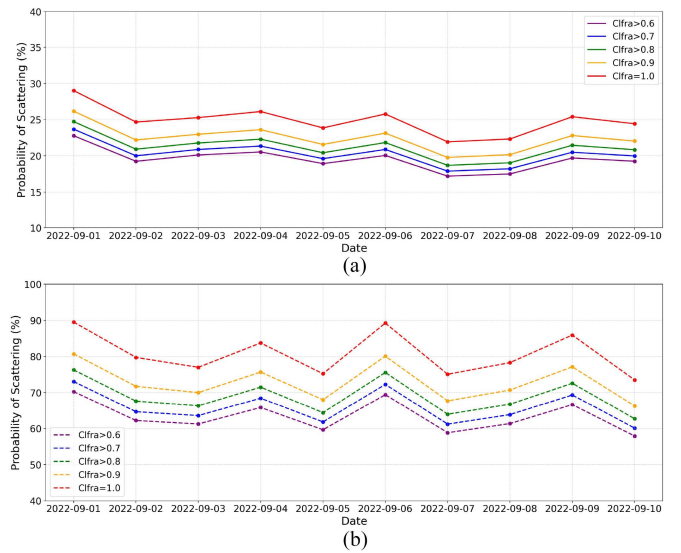


Fig. 3. Temporal evolution of the probability of occurrence of (a) Mie scattering and (b) Rayleigh scattering for different matched Clfra from 1 September to 10 September 2022. The lines in the figure represent the ratio of the number of pixels from (a) Mie scattering and (b) Rayleigh scattering to the number of pixels with different matching Clfra.

to the number of pixels with different matched Clfra. Global precipitation changes daily, but the total area of precipitation varies little, hence the probability of Mie scattering under different matched Clfra remains relatively stable over time. It can be seen that Mie scattering is positively correlated with the matched Clfra: a Clfra of 0.6, corresponds to a 20% probability of Mie scattering, increasing to 22% at 0.7 and up to 26% at 1.0, indicating higher Clfra corresponds to greater probabilities of Mie scattering. Fig. 3(b) shows the occurrence of Rayleigh scattering. It can be seen that the probability of the matched Clfra

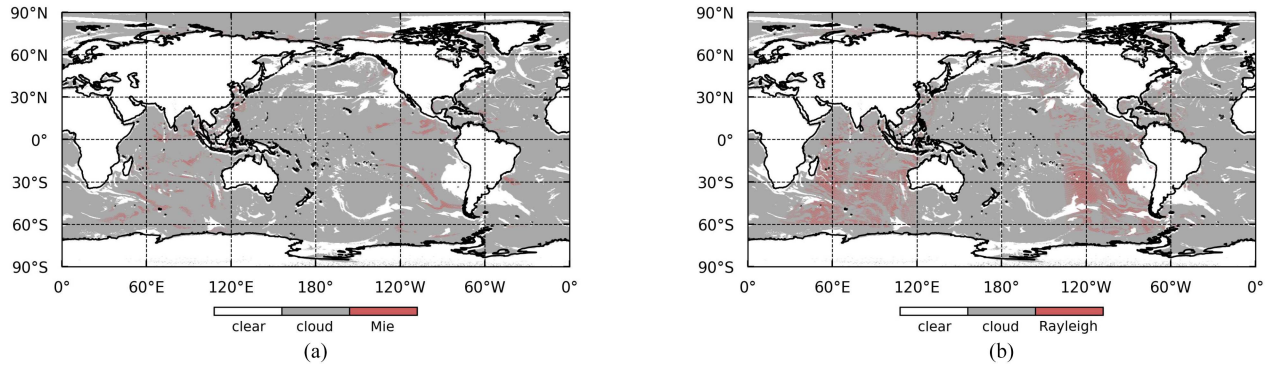


Fig. 4. Experimental region of microwave (a) Mie scattering and (b) Rayleigh scattering determined based on the CMA-GFS 24-h forecast results at 0000 UTC on 3 September 2022. The white area over oceans represents the clear sky, while the white area over lands only represents the continents.

and scattering is higher due to the decrease in the threshold of CLWP, and the distribution trend is almost the same as that in Fig. 3(a). Combining the results from Figs. 2 and 3, all microwave scattering pixels occur in areas where the matched MERSI Clfra is greater than zero. Compared to Mie scattering, Rayleigh scattering requires a smaller effective radius of hydromorphic particles and shows better consistency with the matched MERSI Clfra. Therefore, using the MERSI Clfra matched to MWTS-III FOVs to identify microwave scattering may lead to more false positives, resulting in the exclusion of clear-sky pixels in the microwave spectrum.

B. Consistency Analysis of NWP Model Forecast and MWTS-III Retrieved Scattering At One Single Moment in Time

Typically, the cloud in the NWP model includes five types of hydromorphic particles: cloud water (qc), rain water (qr), cloud ice (qi), snow water (qs), and graupel (qg). In cloud environments, microwave radiation at 60 GHz is mainly affected by the scattering of liquid hydromorphic particles. Fig. 4 shows the global cloud distribution (gray area) of the 24-h forecast from the CMA-GFS model at 0000 UTC on 3 September 2022. When the sum of five types of hydromorphic particles is greater than zero in a certain region, it will be defined as a cloud-cover region. It can be seen that the cloud-cover region accounts for more than 80% of the Earth's surface area in Fig. 4. The red region in the figure is the pixel distribution of Mie scattering [see Fig. 4(a)] and Rayleigh scattering [see Fig. 4(b)] retrieved from MWTS-III. It is observed that since (1) can only retrieve CLWP over the open ocean surface, the regions of Mie and Rayleigh scattering at 60 GHz microwave spectrum are entirely contained within the cloud region of the numerical forecast. The effective radius of the hydromorphic particle in Mie scattering is much larger than that in Rayleigh scattering, the region of Mie scattering is much smaller than that of Rayleigh scattering. Furthermore, the region of Mie scattering is completely encompassed within the Rayleigh scattering region.

When the vertical velocity in the forecast is greater than zero ($w > 0$), the hydromorphic particles in the cloud ascend, potentially reaching the cloud top. The CMA-GFS forecast variables were matched to the closest MWTS-III pixel to the grid point in

the NWP forecast. Fig. 5(a) and (b) shows the distributions of the forecast w at 300, 500, 700, and 850 hPa during MWTS-III Mie scattering versus Rayleigh scattering, respectively. The CMA-GFS field primarily describes atmospheric circulation distribution and has relatively limited simulation capability for medium to small-scale systems like convection. As a result, the maximum w values in the MWTS-III scattering region are less than 1 m/s, with an average of around 10^{-2} m/s. There are no obvious differences in the distribution of w value among pressure layers. In typhoon area (28°N , 125°E), intertropical convergence zone (near 120°W and 70°E), and the westerlies (near 80°W and 90°E), which are the regions affected by the strong scattering of the MWTS-III observations, the w values at all level were greater than 0.1 m/s, and the maximum values were about 0.5 m/s at 300 hPa. The w value in the Mie scattering region is higher than that in the Rayleigh scattering region. Using (7) to calculate the maximum allowable effective particle radius R_p of liquid hydromorphic particles under the constraint of w , the distribution at each pressure layer is shown in Fig. 5(c) and (d). The effective radius of liquid hydromorphic particles is positively correlated with the value of w , with the corresponding effective radius ranging between 0–9 mm. Most Mie scattering regions have a larger effective radius of liquid hydromorphic particles than in the Rayleigh scattering region. But near 45°S , 60°E , the effective radius in the Rayleigh region was in the range of 15–20 mm, which was equivalent to the w in the strong Mie scattering region. This is attributed to the mismatch between the NWP forecast and the observations. The microwave scattering region is entirely contained within the cloud regions simulated by the NWP model. There is a strong correlation between the w values of the upward motion of cloud water particles and the regions experiencing Mie and Rayleigh scattering.

C. Daily Variation of the NWP Model Forecast and the Scattering Distribution of the MWTS-III Retrieval

Using the maximum possible effective radius R_p of the liquid hydromorphic particles calculated by (7), and assuming that there is no entrainment, coagulation, and no phase transition during the vertical motion, the maximum possible equivalent

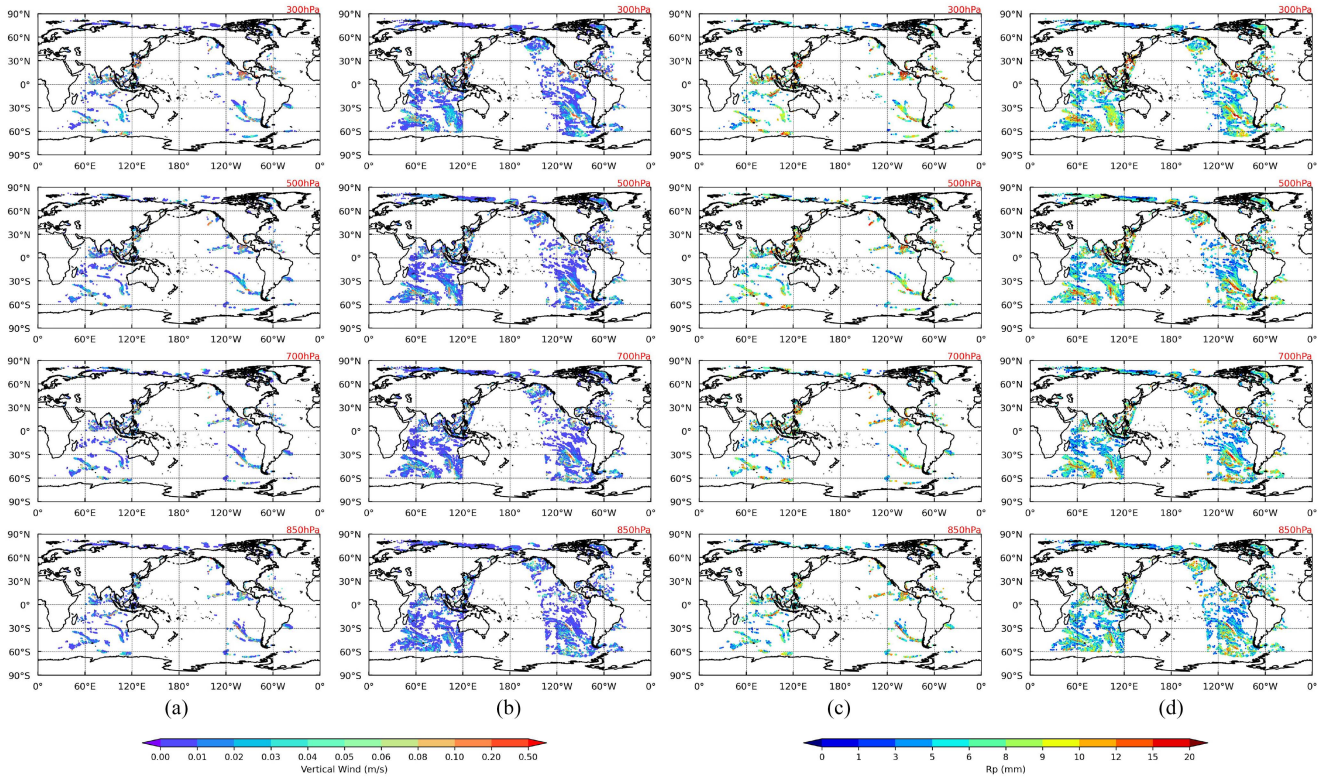


Fig. 5. (a), (b) Vertical velocities w and (c), (d) inverted particle radius R_p at 300, 500, 700, and 850 hPa of the CMA-GFS 24-h forecast at 0000 UTC on 3 September 2022, for (a), (c) Mie scattering and (b), (d) Rayleigh scattering.

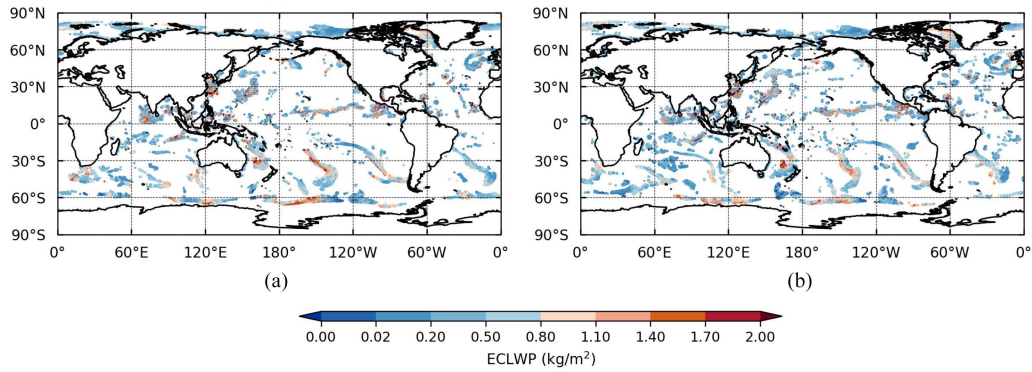


Fig. 6. ECLWP of (a) ascending orbit and (b) descending orbit for the Mie scattering simulated from the CMA-GFS 24-h forecast at 0000 UTC on 3 September 2022.

CLWP (ECLWP) of the liquid hydromorphic particles is obtained by integrating the atmospheric layers below 300 hPa:

$$\text{ECLWP} = \int_0^z D_p \rho_{\text{wet}} dz = \sum_0^z D_p \rho_{\text{wet}} \delta z \quad (8)$$

where D_p is the diameter of the liquid hydromorphic particles and ρ_{wet} is the mixing density of the wet air, derived from the CMA-GFS forecast. The 24-h global forecast at 0000 UTC on 3 September 2022, was matched to MWTS-III pixels. The ascending and descending orbit distributions of the ECLWP for Mie scattering diagnosed by (8) are shown in Fig. 6(a)

and (b). For the Mie scattering region, the ECLWP distributed in $[0.0002 \text{ kg/m}^2, 2.0 \text{ kg/m}^2]$, and the maximum value was much larger than the minimum value of CLWP (0.2 kg/m^2) at 60 GHz retrieved by (1). This is because the actual effective radius of liquid hydromorphic particles in the atmosphere follows a specific spectral distribution, and the CLWP retrieved under the constraints of these spectral distributions is much lower than the ECLWP constrained by the rectangular spectrum with the largest particle effective radius. On the other hand, the minimum simulated ECLWP is much smaller than 0.2 kg/m^2 . It can be seen that for both ascending and descending orbits, the probability of the ECLWP being smaller than 0.2 kg/m^2 is less than 5%,

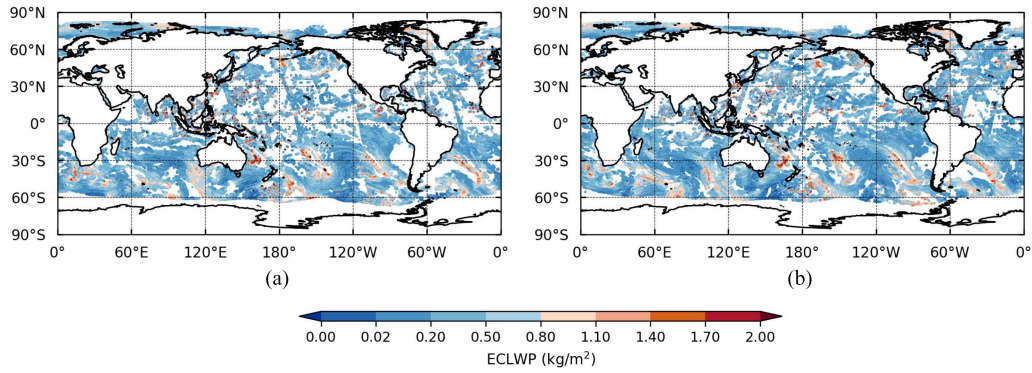


Fig. 7. ECLWP of (a) ascending orbit and (b) descending orbit for the Rayleigh scattering simulated from the CMA-GFS 24-h forecast at 0000 UTC on 3 September 2022.

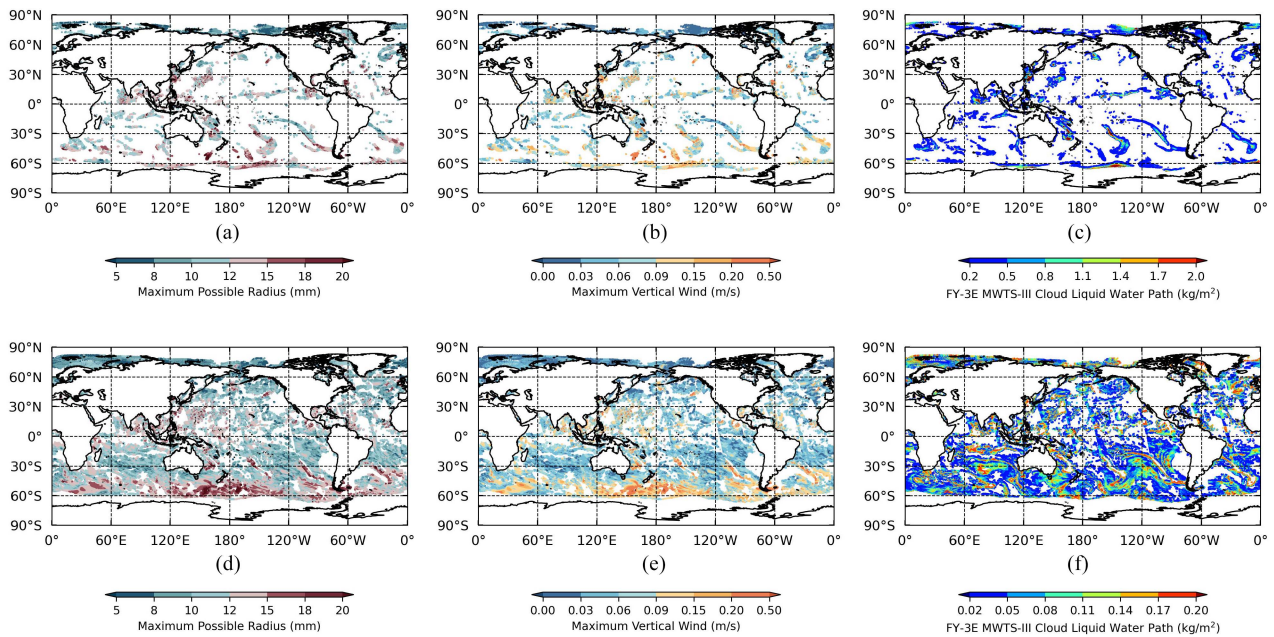


Fig. 8. (a), (d) Maximum possible particle radius R_p , (b), (e) Maximum vertical velocity w of the whole atmosphere in the CMA-GFS forecast, and (c), (f) CLWP retrieved from FY-3E MWTS-III observations for (a), (b), (c) Mie and (d), (e), (f) Rayleigh scattering experiment region based on the CMA-GFS 24-h forecast results at 0000 UTC on 3 September 2022.

which suggests that discrepancies between ECLWP and observed Mie scattering regions are minimal and can be attributed to differences between NWP model forecasts and observation. In addition, this indicates that the distribution of hydromorphic particles in the CMA-GFS forecast is in good agreement with the Mie scattering distribution of FY-3E MWTS-III.

Fig. 7(a) and (b) shows the Rayleigh scattering distributions of the two orbits. The analysis of Rayleigh scattering is similar to that of Mie scattering. The range of ECLWP values is similar to the Mie scattering, which was $[0.0001 \text{ kg/m}^2, 2.0 \text{ kg/m}^2]$. Approximately 96% of the pixels over the ocean had an ECLWP greater than 0.02 kg/m^2 , which indicates good consistency between hydromorphic particle distribution in the CMA-GFS forecast and the Rayleigh scattering distribution observed by MWTS-III. However, a small fraction of pixels particularly in westerlies, exhibit ECLWP values larger than those during Mie

scattering, primarily occurring in the region at the edge of the orbit with a strong edge effect. The distribution of the other part is the same as that in Fig. 6, with similar causal factors. These pixels constitute less than 1% of the total and their impact can be considered negligible. To sum up, regardless of whether it is Mie or Rayleigh scattering, and whether it is the ascending or descending orbit, the distribution of hydrometeors in the CMA-GFS forecast is in good agreement with the scattering distribution of the MWTS-III retrieval.

In the case of Mie scattering in the cloud area simulated from the 24-h forecast of CMA-GFS, the maximum possible effective particle radius of the hydromorphic particle is shown in Fig. 8(a), and the predicted maximum w ($w > 0$) in the whole atmosphere is shown in Fig. 8(b), and the CLWP distribution of the MWTS-III retrieval is shown in Fig. 8(c). The corresponding variables distributions within the ascending orbit of Rayleigh

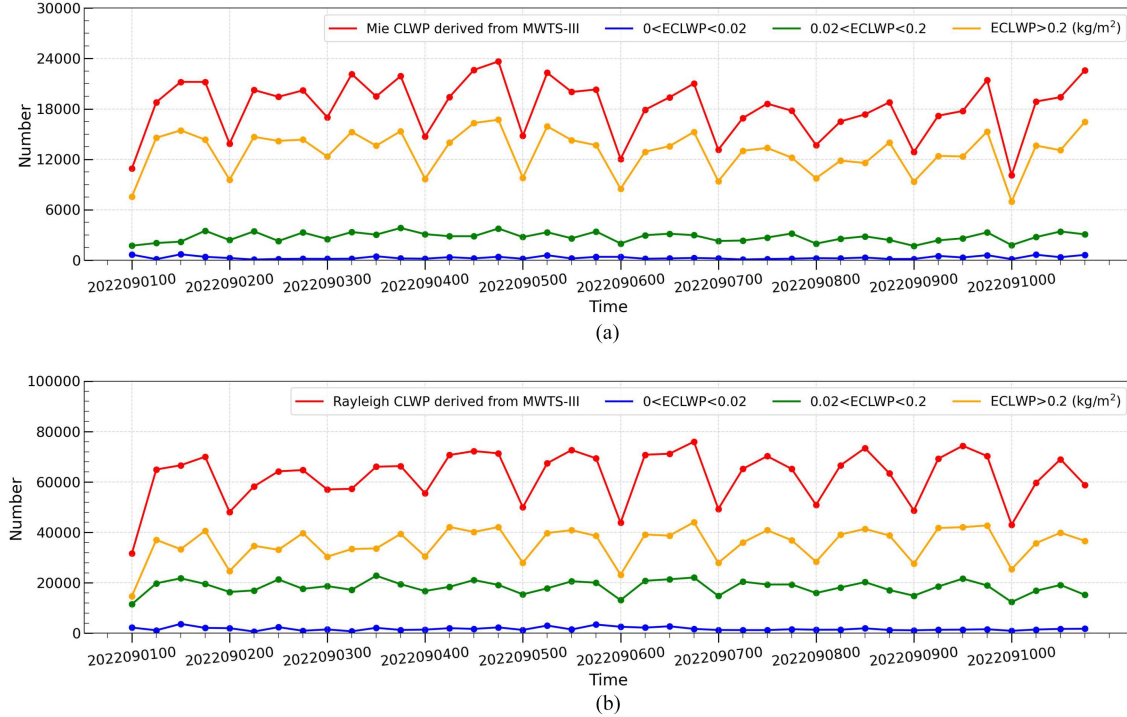


Fig. 9. Time series analysis of the ECLWP in (a) Mie and (b) Rayleigh scattering from 1 September 2022, to 10 September 2022. The red lines represent the CLWP derived from MWTS-III during Mie or Rayleigh scattering. There are four times for each date: 0000, 0600, 1200 and 1800 UTC. “2022090100” means 0000 UTC on 1 September 2022, “2022090200” means 0000 UTC on 2 September 2022, and so on for other dates.

scattering are shown in Fig. 8(d)–(f). The figures demonstrate good consistency in the distribution of the maximum possible effective particle radius of hydromorphic particles, the maximum w for the entire atmosphere in the CMA-GFS forecast, and the retrieved CLWP regardless of whether it is Mie or Rayleigh scattering. Moreover, there is a strong positive correlation between the maximum vertical velocity w , the maximum possible effective particle radius R_p of the whole atmosphere in the CMA-GFS forecast, and CLWP. For example, when w is greater than 0.5 m/s in the typhoon area of the East China Sea, the corresponding maximum R_p is greater than 20 mm, and the CLWP value is about 1.7–2.0 kg/m². However, in the Rayleigh scattering region, particularly in the westerlies, South Indian Ocean, and the South Pacific, there is vertical motion of the same magnitude as in the Mie scattering region, with the maximum possible R_p of hydromorphic particles also around 20 mm, but the CLWP value does not exceed 0.2 kg/m². Therefore, the content of hydrometeors in the NWP model is significantly overestimated compared to the observed CLWP.

D. Time Series Analysis of the NWP Model Forecast and the Scattering Distribution of the MWTS-III Retrieval

In the daily statistics from 1 September 2022, to 10 September 2022, CMA-GFS produced a 24-h forecast every 6 h. Fig. 9(a) compares the retrieved CLWP from MWTS-III and ECLWP during Mie scattering, which shows a clear daily variation in the number of CLWP samples, with the smallest number

at 0000 UTC each day, and the maximum difference in number can be more than double. The situation for ECLWP > 0.2 kg/m² is similar, which also shows obvious diurnal variation, but the number of samples is less than that of the retrieved CLWP. The number of all ECLWP > 0 samples is the same as that of the retrieved CLWP, but only 75% of the ECLWP samples were coincident with the observed samples in the Mie scattering environment (CLWP > 0.2 kg/m²), which shows that CMA-GFS has limited capability in representing the strong convective system, resulting in about quarter of the samples having the maximum possible ECLWP is lower than the Mie scattering threshold, indicating the value of vertical velocity w is too small. The Rayleigh scattering in Fig. 9(b) is similar to that in Fig. 9(a). Approximately 30% of the ECLWP samples were distributed between 0.02 and 0.2 kg/m², with over 50% of the samples being larger than 0.2 kg/m². The results show that there is little difference between ECLWP and the observed values in the Rayleigh scattering environment, suggesting CMA-GFS’s representation of weak convection had better adaptability in the Rayleigh scattering environment.

Fig. 10 shows the daily statistics of the vertical velocity w in the CMA-GFS forecast and the maximum possible effective radius R_p of hydromorphic particles, as well as their relationship with the number of retrieved CLWP in two scattering environments. It can be found that when describing the Mie scattering environments, and according to the statistics of the maximum possible effective radius of hydromorphic particles, the maximum possible R_p values deduced from the CMA-GFS

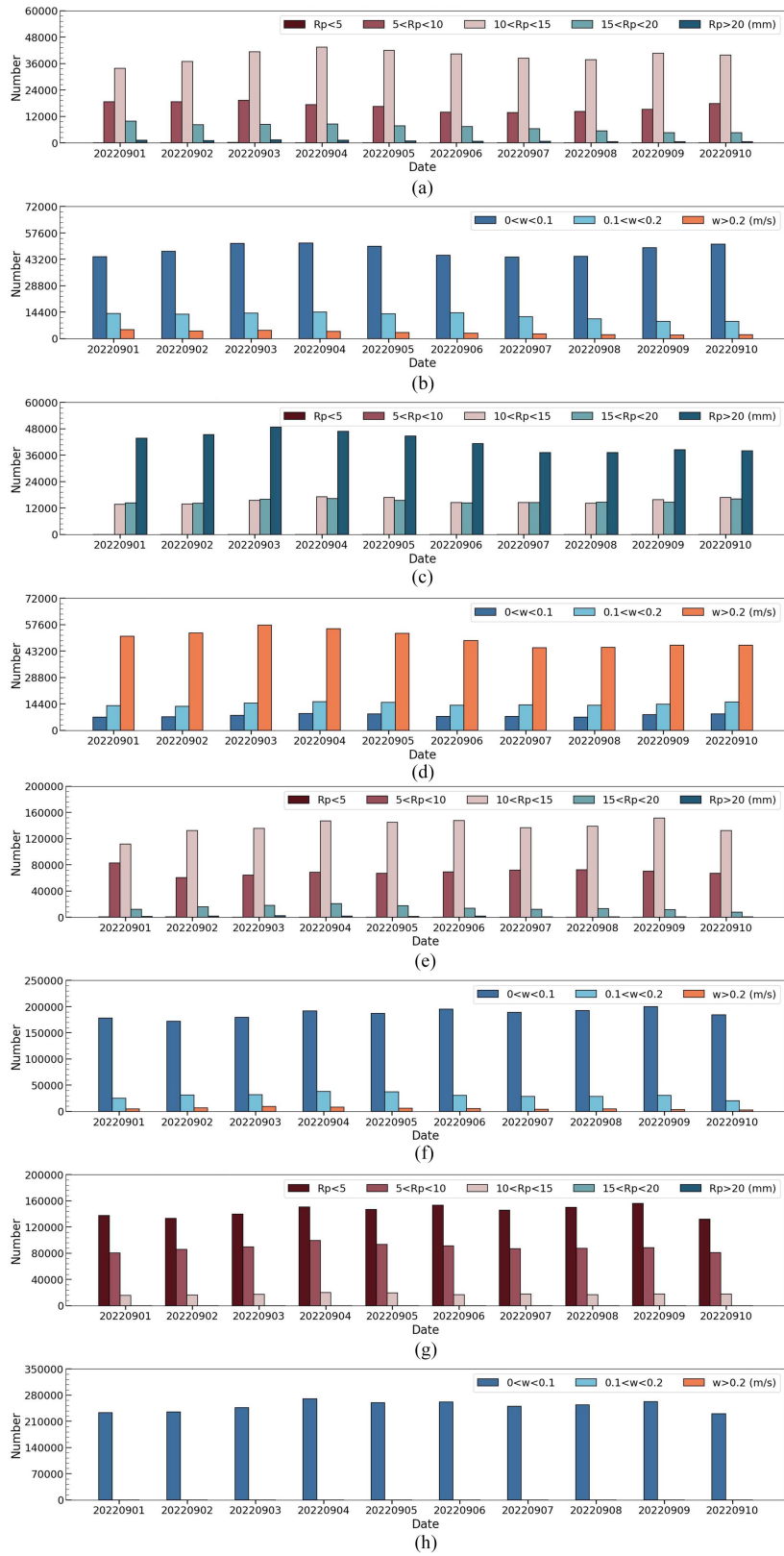


Fig. 10. Temporal evolution of (a), (c), (e), (g) maximum possible particle R_p and (b), (d), (f), (h) maximum vertical winds w for (a), (b), (c), (d) Mie scattering and (e), (f), (g), (h) Rayleigh scattering from 1 September 2022, to 10 September 2022. (a), (e) Maximum possible R_p calculated from the CMA-GFS forecast. (b), (f) Maximum w simulated from the CMA-GFS forecast. (c), (g) Maximum possible R_p deduced from the retrieved CLWP. (d), (h) Maximum possible w deduced from the retrieved CLWP.

forecast were mainly concentrated in the range of 10–15 mm [see Fig. 10(a)]. In contrast, the R_p deduced from the retrieved CLWP is mainly distributed above 10 mm [see Fig. 10(c)], with more than 50% of the samples distributed exceeding 20 mm, indicating a significant difference in the distribution trend between them. In Fig. 10(b), the samples with $w > 0$ mainly fall within the 0–0.1 m/s range, accounting for more than 50% of the total. Samples with $w > 0.2$ m/s and in the range of 0.1–0.2 m/s are less than half of the total, which is contrary to the maximum possible w value deduced from the retrieved CLWP in Fig. 10(d). Fig. 10(e)–(h) shows the daily statistical results of w and R_p in the Rayleigh scattering environment. Rayleigh scattering allows for the presence of smaller-diameter hydromorphic particles and has a broader range of w -value thresholds. Thus, the number of samples with w ranging in 0–0.1 m/s in Fig. 10(f) accounts for the vast majority of the total number of samples, showing good consistency with the maximum w value derived from the retrieved CLWP [see Fig. 10(h)]. The distribution of R_p in Fig. 10(e) is not as obvious as that of w , but similar to the Mie scattering scenario, showing a significant difference from the maximum possible R_p derived from the retrieved CLWP in Fig. 10(g). The comprehensive analysis shows that the vertical motion field predicted by CMA-GFS is different from the vertical motion derived from satellite observations because of the difference between the particle spectrum hypothesis and the model. The simulated w shows better consistency with retrieved scattering in the Rayleigh scattering environment, but there is a larger error in the Mie scattering scenario.

V. CONCLUSION

Conducting precipitation detection from satellite microwave observations and excluding data contaminated by scattering from hydromorphic particles can effectively improve the analysis accuracy of NWP model variables. The induction of microwave scattering is closely related to the effective radius of the hydromorphic particle, and the movement of these particles will change the dynamic structure within clouds, leading to precipitation. Although the distribution of hydromorphic particles in the NWP model space is different from the actual observation, in the overlapping area, the maximum possible effective particle radius of hydromorphic particles can be obtained by dynamic analysis within clouds without phase transition and vertical movement of them. Furthermore, the consistency between CLWP distribution and satellite microwave precipitation detection can be analyzed. This article utilized on-orbit observations of MWTS-III and MERSI carried by the FY-3E platform, combined with the vertical dynamic characteristics of CMA-GFS global numerical forecast in the cloud environment, to evaluate the consistency of CLWP retrieved by FY-3E MWTS-III and multispectral fusion precipitation detection distribution. The conclusions are as follows.

- 1) The cloud fraction data from MERSI were remapped to MWTS-III FOVs. Despite different resolutions, there is good consistency between the cloud distributions from the satellite microwave-sounding data and the satellite visible

near-infrared sounding data. All microwave scattering pixels occur in areas where matched MERSI Clfra is greater than zero. Compared to Mie scattering, Rayleigh scattering shows better consistency with the matched MERSI Clfra, indicating the matched Clfra method is more suitable for Rayleigh scattering.

- 2) The effective radius of the liquid hydromorphic particles is positively correlated with the value of w . The maximum value of w in the scattering region of MWTS-III is less than 1 m/s, with an average value about around 10^{-2} m/s, the corresponding effective radius of the liquid hydromorphic particles is centrally distributed in the range of 0–9 mm.
- 3) Regardless of whether it is Mie or Rayleigh scattering, and whether it is an ascending or descending satellite orbit, the distribution of hydromorphic products in the CMA-GFS forecast is in consistency with that of MWTS-III. However, the CLWP value did not exceed 0.2 kg/m^2 in the Rayleigh scattering region such as westerlies, the Southern Indian Ocean, and the South Pacific Ocean, indicating the content of hydromorphic products in the NWP model is obviously overestimated compared with the CLWP retrieved from the MWTS-III observations.
- 4) The CMA-GFS has limited capability in representing strong convective systems, resulting in around 25% of the samples having a maximum possible ECLWP lower than the Mie scattering threshold of 0.2 kg/m^2 . Whereas the ECLWP in the Rayleigh scattering environment does not differ significantly from the observed value, suggesting the weak convection of CMA-GFS has better adaptability in the Rayleigh environment.

However, this article is based on the assumption of statically suspended hydromorphic particles and a dynamic analysis based on this assumption. The real atmospheric state is rapidly changing and interconverting, influenced by the atmospheric thermodynamic and dynamic processes, with a significantly uneven distribution of atmospheric microphysical particles, primarily caused by cloud and precipitation processes. Therefore, further exploration of the time-varying characteristics of hydromorphic particles in the atmosphere is warranted.

REFERENCES

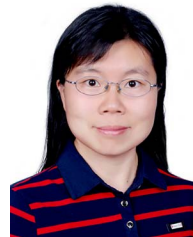
- [1] C. Gu, C. Chen, and W. Guo, "Influence of cloud detection of infrared satellite data on numerical simulation of typhoon," (in Chinese) *Infrared*, vol. 39, no. 1, pp. 24–30, 2018.
- [2] L. Zhu, Z. Qin, and J. Cheng, "A new cloud detection algorithm based on brightness temperature variation for FY-3 C microwave humidity sounder over land," (in Chinese) *Acta Meteorologica Sinica*, vol. 76, no. 3, pp. 434–448, 2018.
- [3] P. Dong et al., "Application status and development of satellite data assimilation in numerical weather forecast," *Meteorol. Sci. Technol.*, vol. 36, no. 1, pp. 1–7, 2008.
- [4] H. Lawrence, N. Bormann, I. Sandu, J. Day, J. Farnan, and P. Bauer, "Use and impact of arctic observations in the ECMWF numerical weather prediction system," *Quart. J. Roy. Meteorol. Soc.*, vol. 145, no. 725, pp. 3432–3454, 2019.
- [5] J. Xue, "Scientific issues and perspective of assimilation of meteorological satellite data," *Acta Meteorologica Sinica*, vol. 67, no. 9, pp. 903–911, 2009.

- [6] S. Liu, P. Dong, W. Han, and W. Zhang, "Simulative study of satellite microwave observation for typhoon Luosha using RTTOV and CRTM and the comparison," *Acta Meteorologica Sinica*, vol. 70, no. 3, pp. 585–597, 2012.
- [7] P. Dong et al., "Application of direct assimilation of FY-3 A microwave detection data and simulation of brightness temperature under cloud and rain conditions," (in Chinese) *J. Trop. Meteorol.*, vol. 30, no. 2, pp. 302–310, 2014.
- [8] Y. Guo et al., "Calibration and validation of microwave humidity and temperature sounder onboard FY-3 C satellite," (in Chinese) *Chin. J. Geophys.*, vol. 58, no. 1, pp. 20–31, 2015.
- [9] X. Zou, F. Weng, B. Zhang, L. Lin, and Z. Qin, "Impacts of assimilation of ATMS data in HWRF on track and intensity forecasts of 2012 four landfall hurricanes," *J. Geophysical Res., Atmospheres*, vol. 118, no. 20, pp. 11–558, 2013.
- [10] X. Zou and Z. Qin, "Development and initial assessment of a new land index for microwave humidity sounder cloud detection," *J. Meteorol. Res.*, vol. 30, no. 1, pp. 12–37, 2016.
- [11] Y. Xie, S. Fan, M. Chen, J. Shi, J. Zhong, and X. Zhang, "An assessment of satellite radiance data assimilation in RMAPS," *Remote Sens.*, vol. 11, no. 1, 2018, Art. no. 54.
- [12] N. Grody, F. Weng, and R. Ferraro, "Application of AMSU for obtaining hydrological parameters," in *Microwave Radiometry and Remote Sensing of the Earth's Surface and Atmosphere*. Boca Raton, FL, USA: CRC Press, pp. 339–352, 2000.
- [13] R. Bennartz, A. Thoss, A. Dybbroe, and D. B. Michelson, "Precipitation analysis using the advanced microwave sounding unit in support of now-casting applications," *Meteorol. Appl.*, vol. 9, no. 2, pp. 177–189, 2002.
- [14] N. Grody, J. Zhao, R. Ferraro, F. Weng, and R. Boers, "Determination of precipitable water and cloud liquid water over oceans from the NOAA 15 advanced microwave sounding unit," *J. Geophysical Res., Atmos.*, vol. 106, no. D3, pp. 2943–2953, 2001.
- [15] F. Weng, L. Zhao, and R. Ferraro, "Advanced microwave sounding unit cloud and precipitation algorithms," *Radio Sci.*, vol. 38, no. 4, pp. 33–1, 2003.
- [16] X. Zou, Z. Qin, and F. Weng, "Improved quantitative precipitation forecasts by MHS radiance data assimilation with a newly added cloud detection algorithm," *Monthly Weather Rev.*, vol. 141, no. 9, pp. 3203–3221, 2013.
- [17] J. Li and X. Zou, "A quality control procedure for FY-3 A MWTS measurements with emphasis on cloud detection using VIRR cloud fraction," *J. Atmospheric Ocean. Technol.*, vol. 30, no. 8, pp. 1704–1715, 2013.
- [18] J. Li and G. Liu, "Assimilation of chinese FY-3B microwave temperature sounder radiances into global GRAPES system with an improved cloud detection threshold," *Front. Earth Sci.*, vol. 10, pp. 145–158, 2015.
- [19] J. Li and G. Liu, "Direct assimilation of chinese FY-3 C microwave temperature Sounder-2 radiances in the global GRAPES system," *Atmospheric Meas. Techn.*, vol. 9, no. 7, pp. 3095–3113, 2016.
- [20] H. Han et al., "Microwave sounder cloud detection using a collocated high-resolution imager and its impact on radiance assimilation in tropical cyclone forecasts," *Monthly Weather Rev.*, vol. 144, no. 10, pp. 3937–3959, 2016.
- [21] J. Sun, "Role of cloud physics in precipitation forecasting by synoptic dynamics," *Meteorol. Monthly*, vol. 40, no. 1, pp. 1–6, 2014.
- [22] B. M. Muller, H. E. Fuelberg, and X. Xiang, "Simulations of the effects of water vapor, cloud liquid water, and ice on AMSU moisture channel brightness temperatures," *J. Appl. Meteorol.*, vol. 33, no. 10, pp. 1133–1154, 1994.
- [23] L. Dennis and V. Johannes, *Physics and Chemistry of Clouds*. Cambridge, U.K.: Cambridge Univ. Press, 2011.
- [24] L. Wang and Y. Fu, "A case study of precipitation along the winter storm track in the north pacific based on the GPM and ERA5 data," *Torrential Rain Disasters*, vol. 41, no. 5, pp. 525–535, 2022.
- [25] Z. Qin, Z. Wu, and J. Li, "Impact of the one-stream cloud detection method on the assimilation of AMSU-A data in GRAPES," *Remote Sens.*, vol. 12, no. 22, 2020, Art. no. 3842.
- [26] Y. Huang, J. Li, and Z. Qin, "Evaluation of the FY-3E microwave temperature sounding data assimilation on forecasting typhoon chanthu (2021)," *Meteorol. Atmospheric Phys.*, vol. 135, no. 6, 2023, Art. no. 54.
- [27] X. Liu and J. Mao, "Statistical relationship between liquid water content and optical thickness of cloud," (in Chinese) *Acta Scientiarum Naturalium Universitatis Pekinensis*, vol. 44, no. 1, pp. 115–120, 2008.
- [28] J. L. Brenguier, F. Burnet, and O. Geoffroy, "Cloud optical thickness and liquid water path—Does the k coefficient vary with droplet concentration?" *Atmospheric Chem. Phys.*, vol. 11, no. 18, pp. 9771–9786, 2011.
- [29] X. Qian, Z. Qin, J. Li, Y. Han, and G. Liu, "Preliminary evaluation of FY-3E microwave temperature sounder performance based on observation minus simulation," *Remote Sens.*, vol. 14, no. 9, 2022, Art. no. 2250.
- [30] M. Zhang et al., "Assessment on unsystematic errors of GRAPES_GFS2.0," (in Chinese) *J. Appl. Meteorol. Sci.*, vol. 30, no. 03, pp. 332–344, 2019.
- [31] J. Wang et al., "Improvements and performances of the operational GRAPES_GFS 3DVar system," (in Chinese) *J. Appl. Meteorol. Sci.*, vol. 28, no. 01, pp. 11–24, 2017.
- [32] A. Arakawa and V. R. Lamb, "Computational design of the basic dynamical processes of the UCLA general circulation model," *Gen. Circulation Models Atmos.*, vol. 17, no. Supplement C, pp. 173–265, 1977.
- [33] J. Xue and D. Chen, *Scientific Design and Application of Numerical Prediction System GRAPES*. Beijing, China: Science Press, 2008.



Yuxuan Feng was born in Shaanxi Xi'an, China. She received the B.S. degree in aerospace science and technology from Xidian University, Xi'an, China, in 2022. She is currently working toward the master's degree in microwave atmospheric detection from the University of Chinese Academy of Sciences, Beijing, China.

Her research interests include the processing and application of microwave remote sensing information, and the characteristics of atmospheric hydrometeors.



Jieying He (Member, IEEE) received the Ph.D. degree in computer science and applied research from the National Space Science Center, Chinese Academy of Sciences, Beijing, China, in 2012.

She is currently the Deputy Chief Designer of microwave humidity sounder for FengYun-3 satellite and salinity radiometer for Haiyang satellites, and the Leader of the conceptual research project of the Space Science (Phase II) Mission. Her research focuses on the design and development of satellite-based microwave radiometer, calibration, and quantification

retrievals for Earth and planetary exploration.

Dr. He is one of the 9th/10th China-U.S. Young Leaders in Space Science, and an Excellent Member of the Youth Innovation Promotion Association of Chinese Academy of Sciences.



Gang Ma received the master's and Ph.D. degrees in data assimilation in short-term numerical weather prediction from the College of Atmospheric Science, Lanzhou University, Lanzhou, China, in 1998 and in 2008, respectively.

He is a Professor of CMA Earth System Modeling and Prediction Centre since 2022, the Deputy Director of the designer to Product Generation System of FY-3 from 2009 to 2017, the Deputy Director of the designer to Simulation and Technique Support System of FY-3 from 2018 to 2021. His research

interests focus on satellite data retrieval and assimilation, fast radiative transfer for satellite data simulation in infrared and microwave bands. He has the intensive experience in developing fast forward operator and techniques to support FY-3/4 satellite data assimilation into operational Numerical Weather Forecasting model in CMA.



Jing Huang received the Ph.D. degree in satellite data assimilation from the College of Atmospheric Science, Lanzhou University, Lanzhou, China, in 2006.

Her research interests focus on satellite data retrieval and assimilation, especially for hyperspectral infrared sounder. She has the intensive experience in developing assimilation key techniques to support FY-3D/3E HIRAS and AIRS, CrIS satellite data assimilation into operational Numerical Weather Forecasting model in CMA.



Guiqing Liu received the master's degree in atmospheric physics and atmospheric environment from the School of Physics, Peking University, Beijing, China, in 2003.

Her research focuses on data preprocessing of satellite data assimilation of vertical sounding data in CMA-GFS. She has extensive experience in satellite data quality control. She is currently an Engineer at the CMA Earth System Modelling and Prediction Centre.



Jingyang Li received the M.S. degree in geographical and cartographical science from George Mason University, Fairfax, VA, USA, in 2023.

Her current research primarily focuses on the integration of infrared and microwave remote sensing, along with hyperspectral microwave remote sensing analysis.



Peng Zhang (Senior Member, IEEE) received the M.S. degree in atmospheric optics from the Anhui Institute of Optics and Fine Mechanics, Chinese Academy of Sciences, Hefei, China, in 1995, and the Ph.D. degree in atmospheric physics from the Institute of Atmospheric Physics, Chinese Academy of Sciences, Beijing, China, in 1998.

He has been the Deputy Director-General of the National Satellite Meteorological Center, Beijing, China, since 2013. He has been the Chief Director of the FY-3 ground segment and Chinese TanSat satellite ground segment since 2013 and 2015, respectively. He was the Chair of the Global Space Inter-Calibration System Executive Panel from 2014 to 2017. His research interests include atmospheric remote sensing, satellite data assimilation, satellite calibration, and validation. He has intensive experience in conceiving, developing, and operating the FY-3 satellite ground segment.



Yang Guo received the B.S. degree in atmospheric science from Nanjing University of Information Science and Technology, Nanjing, China, in 2006 and the Ph.D. degree in atmospheric physics from the Nanjing University of Information Science and Technology, Nanjing, China, in 2019.

She is currently a Senior Scientist with the National Satellite and Meteorological Center, China Meteorological Administration, Beijing. As the Instrument Scientist of Microwave Humidity Sounder, the major fields that she is working on include calibration and validation, quality control and data assimilation for MWHS.



Jiandong Gong received the master's and Ph.D. degrees in atmospheric science from Lanzhou University for Meteorology, Lanzhou, China, in 1996 and 1999, respectively.

He is the Deputy Director General of the Center for Earth System Modeling and Prediction of CMA since 2021. His major field focuses on the data assimilation.